Biogeosciences, 20, 2265–2282, 2023
https://doi.org/10.5194/bg-20-2265-2023

Biogeosciences Open Access EGU

Mapping of ESA's Climate Change Initiative land cover data to plant functional types for use in the CLASSIC land model

Libo Wang[1], **Vivek K. Arora**[2], **Paul Bartlett**[1], **Ed Chan**[1], **and Salvatore R. Curasi**[3,4]

[1]Climate Processes Section, Climate Research Division, Environment and Climate Change Canada, Toronto, ON, Canada
[2]Canadian Centre for Climate Modelling and Analysis, Climate Research Division,
Environment and Climate Change Canada, Victoria, BC, Canada
[3]Department of Geography and Environmental Studies, Carleton University, Ottawa, ON, Canada
[4]Climate Processes Section, Climate Research Division, Environment and Climate Change Canada, Victoria, BC, Canada

Correspondence: Libo Wang (libo.wang@ec.gc.ca)

Received: 14 September 2022 – Discussion started: 4 October 2022
Revised: 17 March 2023 – Accepted: 8 May 2023 – Published: 20 June 2023

Abstract. Plant functional types (PFTs) are used to represent vegetation distribution in land surface models (LSMs). Previous studies have shown large differences in the geographical distribution of PFTs currently used in various LSMs, which may arise from the differences in the underlying land cover products but also the methods used to map or reclassify land cover data to the PFTs that a given LSM represents. There are large uncertainties associated with existing PFT mapping methods since they are largely based on expert judgement and therefore are subjective. In this study, we propose a new approach to inform the mapping or the cross-walking process using analyses from sub-pixel fractional error matrices, which allows for a quantitative assessment of the fractional composition of the land cover categories in a dataset. We use the Climate Change Initiative (CCI) land cover product produced by the European Space Agency (ESA). Previous work has shown that compared to fine-resolution maps over Canada, the ESA-CCI product provides an improved land cover distribution compared to that from the GLC2000 dataset currently used in the CLASSIC (Canadian Land Surface Scheme Including Biogeochemical Cycles) model. A tree cover fraction dataset and a fine-resolution land cover map over Canada are used to compute the sub-pixel fractional composition of the land cover classes in ESA-CCI, which is then used to create a cross-walking table for mapping the ESA-CCI land cover categories to nine PFTs represented in the CLASSIC model. There are large differences between the new PFT distributions and those currently used in the model. Offline simulations performed with the CLASSIC model using the ESA-CCI-based PFTs show improved winter albedo compared to that based on the GLC2000 dataset. This emphasizes the importance of accurate representation of vegetation distribution for realistic simulation of surface albedo in LSMs. Results in this study suggest that the sub-pixel fractional composition analyses are an effective way to reduce uncertainties in the PFT mapping process and therefore, to some extent, objectify the otherwise subjective process.

1 Introduction

Land cover is a critical component of the Earth system that affects the exchange of energy, water, and carbon between the land surface and the atmosphere (Pielke et al., 1998; Sterling et al., 2013). Accurate representation of global land cover (LC) is important for land surface models (LSMs), which provide the lower boundary conditions to the atmosphere in numerical weather forecasting, climate, and Earth system models (ESMs). Plant functional types (PFTs) are groups of plant species that share similar structural, phenological, and physiological traits and have been commonly used in LSMs to represent vegetation distribution. This simplification has allowed the simulation of structural attributes of vegetation dynamically within ESMs (Arora and Boer, 2010; Bonan et al., 2003; Krinner et al., 2005). In order to improve the representation of ecosystem ecology and vegetation demographic processes within ESMs, both species-

based and trait-based models have been attempted in LSMs (Fisher et al., 2018; Zakharova et al., 2019). However, these individual-based models are computationally too expensive to model biogeochemical processes, especially photosynthesis and the carbon cycle at the global scale (Bonan et al., 2002; Smith et al., 1997, 2001). As a compromise, "cohort-based" models have been developed where individual plants with similar properties (size, age, functional type) are grouped together and have been implemented in some ESMs (Fisher et al., 2018). Though there are limitations in PFT-based models (Scheiter et al., 2013; Zakharova et al., 2019), PFTs are commonly used in LSMs that participate routinely in the Global Carbon Project (Friedlingstein et al., 2020) and in ESMs that participate in the Coupled Models Intercomparison Project (CMIP, Wang et al., 2016).

There are three approaches for modelling PFTs: (1) static, where the fractional coverage of PFTs is prescribed and does not vary through time; (2) forced, where the fractional coverage of PFTs is still prescribed but vary through time based on scenarios of land-cover/land-use change; and (3) dynamic, where the fractional coverage of PFTs is simulated dynamically with competition for available space and resources between PFTs (Fisher et al., 2018; Melton and Arora, 2016). The number and type of PFTs used in each LSM differ. Global land cover datasets are typically used to derive the fractional coverage of PFTs for use in LSMs. However, large differences exist in both the fractional coverage and the geographical distribution of PFTs, which are caused by differences in the LC datasets themselves but also due to the methods used to map LC datasets to the PFTs represented in various models (Fritz et al, 2011; Hartley et al., 2017; Ottle et al., 2013; Wang et al., 2016).

Since different PFTs are characterized by different physical and biogeochemical processes and parameter values, the spatial distribution and fractional cover of PFTs constitute one of the important geophysical fields that are required for realistic simulation of carbon, water, and energy budgets in LSMs (Arora and Boer, 2010; Betts, 2001). For example, the surface roughness for short or tall vegetation is very different, which affects simulated turbulent exchanges. The surface albedos for needleleaf evergreen trees, broadleaf deciduous trees, and grasslands are also very different, especially during winter when deciduous trees are leafless and short vegetation is largely buried by snow (Bartlett and Verseghy, 2015; Moody et al., 2007). Wang et al. (2016) found that the bias in winter albedo in selected boreal forest regions among the CMIP5 models was largely related to biases in leaf area index (LAI) and tree cover fraction. Model experiments using the MPI-ESM by Georgievski and Hagemann (2019) suggested that uncertainties in vegetation distribution may lead to noticeable variations in near-surface climate variables and large-scale circulation patterns.

The Canadian Land Surface Scheme Including Biogeochemical Cycles (CLASSIC) is an open-source community land model that is designed to address research questions that explore the role of the land surface in the global climate system (Melton et al., 2020). It is the successor to the coupled modelling framework based on the Canadian Land Surface Scheme (CLASS; Verseghy, 1991, 1993) and the Canadian Terrestrial Ecosystem Model (CTEM; Arora and Boer, 2005; Melton and Arora, 2016). The physics and biogeochemistry modules of CLASSIC are based on CLASS and CTEM models, respectively. Since the development of CTEM in the early 2000s, the GLC2000 LC product has been used to specify the spatial distribution of PFTs for CLASSIC when employed as the land surface component of the Canadian Earth system model developed by Environment and Climate Change Canada (Arora et al., 2009; Wang et al., 2006). The Climate Change Initiative (CCI) LC product recently produced by the European Space Agency (ESA) is available at an annual temporal resolution for the period 1992 to 2018 at 300 m spatial resolution (ESA, 2017). It was produced based on broad user consultation, specifically to address the needs of the climate modelling community (Bontemps et al., 2012). Wang et al. (2019) showed that when compared to the finer-resolution maps over Canada, the 300 m ESA-CCI product provides much improved LC distribution over Canada compared to that from the 1 km GLC2000 dataset.

To map LC classes to PFTs, a cross-walking table (CW-table) is usually created to assign fractions of each LC class to the different PFTs, such that the sum of the fractions for each class is always 1 (including fractions of water and bare ground). Previous methods for creating such CW-tables are mainly based on LC class descriptions, expert knowledge, and the spatial distribution of global biomes (Ottle et al., 2013; Poulter et al., 2011, 2015; Sun and Liang, 2007; Wang et al., 2006). Because LC maps only provide the types of vegetation, and each class can be associated with a broad range of fractional cover of either one or more vegetation types, there are large uncertainties associated with any cross-walking or reclassification process. Wang et al. (2019) reclassified the 10 PFTs in the default CW-table provided in the ESA-CCI LC product user manual (Table 7-2, ESA, 2017) into PFTs represented in the CLASSIC model and compared them with those based on the GLC2000 dataset. The results suggest that uncertainties in the CW-tables were a major source of large differences in the PFT distributions. In addition, the fractional coverage of tree PFTs based on the default CW-table for the ESA-CCI LC dataset was overestimated along the taiga–tundra transition zone in western Canada, which led to underestimation in winter albedo in CLASSIC offline simulations driven with observation-based reanalysis data (Wang et al., 2018).

The objective of this study is to develop a new CW-table for reclassifying the ESA-CCI LC classes into PFTs represented in the CLASSIC model over the model's Canadian domain and to compare and assess the performance of CLASSIC offline simulations using the new and existing PFT distributions. Given the close link between the bias in winter albedo and the vegetation distribution in the models (Wang

et al., 2016), our assessment of model performance focuses on the simulated surface albedo during the maximum snow accumulation period (February–March for the boreal forest). This simplifies our analyses by excluding the fall–spring transition periods when biases in snow accumulation and melt timing can have a large influence on surface albedo simulated by LSMs (Wang et al., 2014). In addition, we extend the CW-table for the ESA-CCI LC dataset to the global domain. A comprehensive assessment of the impact of the PFT distribution based on the new CW-table and the ESA-CCI LC dataset on the performance of the CLASSIC model at the global scale is presented in Arora et al. (2022).

2 Data and the CLASSIC model

2.1 The hybrid LC map over Canada

The United States Geological Survey archive of Landsat imagery has provided open and free access to georeferenced and spectrally corrected analysis-ready imagery (Wulder et al., 2012), which makes it possible to generate time series of LC maps to study LC change. Recently two of these products based on Landsat imagery were generated over Canada, including the North America Land Change Monitoring System (NALCMS) LC dataset (Latifovic et al., 2017) and the Virtual Land Cover Engine (VLCE) framework-generated LC dataset (Hermosilla et al., 2018).

Based on the random forest algorithm and local optimization method, the Canada Centre for Remote Sensing has generated the NALCMS LC maps of Canada for the years 2010 and 2015 at 30 m resolution using Landsat imagery (Latifovic et al., 2017). These LC products are the Canadian contribution to the 30 m resolution 2010/2015 LC map of North America to the joint collaborative effort by the Mexican, American, and Canadian government institutions under the NALCMS umbrella. The NALCMS LC map has 19 classes based on the United Nations Land Cover Classification System (LCCS; Di Gregorio, 2005). Assessment based on reference samples showed an overall accuracy of 76.6 % for the year 2010 data (Latifovic et al., 2017), which is used in this study.

VLCE is an automated framework to enable change-informed annual LC mapping using time series of Landsat surface reflectance. Temporally consistent annual LC maps representative of Canada's forested ecosystems from 1984 to 2012 were generated using the VLCE framework, characterizing LC dynamics following wildfire and harvesting events by Hermosilla et al. (2018). The VLCE maps have 12 LC classes in a hierarchical classification structure following that of the National Forest Inventory. Assessment based on reference samples showed an overall accuracy of 70.3 % for the map of the year 2005 (the year with the greatest number of reference samples; Hermosilla et al., 2018). Land cover data from the year 2010 are used in this study.

Overall, the 19-class NALCMS product presents a more detailed LC distribution than the 12-class VLCE map over Canada. For example, areas classified as "exposed/barren lands" in the VLCE map correspond to either "sub-polar or polar grassland–lichen–moss", "sub-polar or polar barren–lichen–moss", or "barren lands" in the NALCMS map. Areas of cropland are not separated from grassland in the VLCE map. A recent study showed that the wetland class in NALCMS suffers from large uncertainty in forest cover mapping because treed–wetland was not separated from herbaceous wetland in its legend (Wang et al., 2019). To take advantage of both datasets, we created a hybrid product by combining them through the following steps: (1) reproject the VLCE data from its Lambert conformal conic projection to the same Lambert azimuthal equal area projection that is used for the NALCMS data; (2) replace pixels classified as "exposed/barren lands" and "bryoids" in the VLCE data with the more specific LC classes from the NALCMS data; (3) replace pixels classified as "herbs" in the VLCE data with the "cropland" class in the NALCMS data (remains "herbs" if not classified as "cropland" in NALCMS); (4) and merge the rest of LC classes from NALCMS to the corresponding classes in the VLCE data. There are a total of 17 classes in this new hybrid product, which we will henceforth refer to it as the hybrid LC dataset and is shown in Fig. 1.

2.2 The global LC products

The GLC2000 dataset was generated from SPOT/VEG data collected from November 1999 to December 2000 at 1 km resolution (Bartholomé and Belward, 2005). It was produced by 21 separate regional expert groups using an unsupervised image classification method. Based on the LCCS, the regional products were merged into one global product with a generalized LCCS legend of 22 classes. Assessment based on a random sampling of reference sites globally estimated an overall accuracy of 68.6 % for the GLC2000 product (Mayaux et al., 2006).

The annual ESA-CCI LC data at 300 m resolution are available for the period 1992–2018, which were generated from baseline data and annual LC changes (ESA, 2017). The baseline data were generated using a combination of machine learning and unsupervised image classification methods from the entire archive of ENVISAT/Medium Resolution Imaging Spectrometer for the period of 2003–2012. The annual LC changes were detected at 1 km resolution from the Advanced Very High Resolution Radiometer time series between 1992 and 1999, SPOT/VEG time series between 1999 and 2013, and the PROBA-V time series between 2013 and 2018. Based on the LCCS legend, the ESA-CCI LC data have 22 level-1 classes, and 15 level-2 sub-classes. Assessment based on the GlobCover validation database estimated an overall accuracy of 71 % for the ESA-CCI LC product (ESA, 2017).

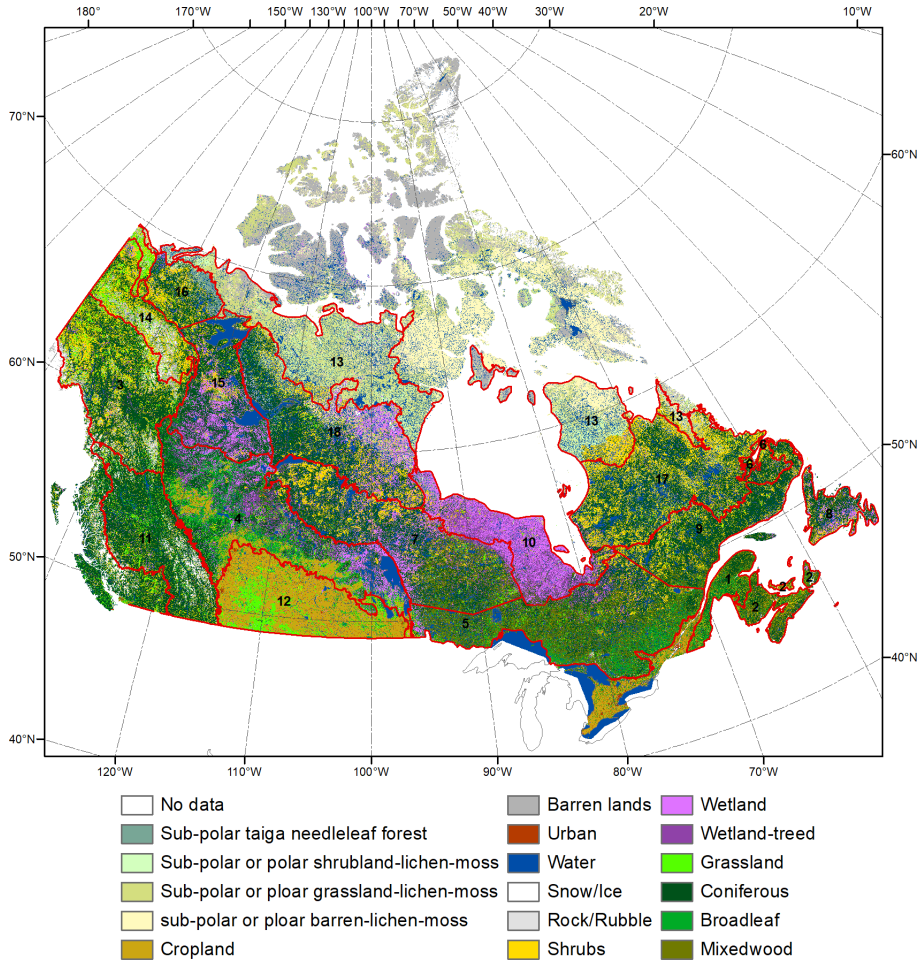

Figure 1. The hybrid land cover map of Canada based on VLCE and NALCMS land cover maps for 2010. The red polygons represent 18 ecozones used in this study.

2.3 Other datasets

Airborne lidar has been used to monitor forests since the 1980s and is well suited to estimate vegetation height, volume, and biomass (Hopkinson et al., 2006; Wulder et al., 2008). Vegetation cover percentage for canopy height above 2 m from airborne lidar data is used to estimate the fraction of tall versus low vegetation for LC classes with a mix of woody and herbaceous vegetation in this study. The lidar data were collected along 34 survey flights across the boreal forest of Canada in the summer of 2010 by the Canadian Forest Service (Wulder et al., 2012). A 25 by 25 m tessellation was generated with the approximately 400 m wide lidar swath, with each cell treated as an individual lidar plot.

A tree cover fraction (TCF) dataset for 2010 is also used in this study (Hansen et al., 2013; hereafter the Hansen TCF dataset). It was based on Landsat images at 30 m resolution. In contrast to the discrete LC classification datasets (providing a certain number of LC classes) as described above, the Hansen dataset is a vegetation continuous field product (providing tree cover fractions from 0 %–100 %), in which the satellite spectral information was used to estimate the TCF in each pixel using a regression tree algorithm (Hansen et al., 2002, 2010). This may better represent heterogeneous areas than is possible by discrete LC classification. Tree cover is defined to exist over pixels where canopy closure is observed for vegetation taller than 5 m in height. Forests are generally defined as woody vegetation taller than 3 m in the regional and global LC datasets. The different definitions of tree heights should not result in much difference in areas with mature forests, such as most boreal forests in Canada.

Simulated surface albedo by the CLASSIC model in offline experiments is evaluated against the Moderate Resolution Imaging Spectroradiometer (MODIS) (MCD43C3) broadband (0.3–5.0 µm) white-sky albedo (Schaaf et al., 2002), with quality flags of 0–2 (75 % or more full inversions and 25 % or fewer fill values) and solar zenith angles less than 70°. The MODIS albedo product used in this study is at 0.05° resolution and is regridded to the 0.22° resolution used for the CLASSIC simulations (see Sect. 2.4.2).

2.4 The CLASSIC model and simulation setup

2.4.1 The CLASSIC model

CLASSIC is the successor to the coupled modelling framework based on the Canadian Land Surface Scheme (CLASS; Verseghy, 1991, 1993) and the Canadian Terrestrial Ecosystem Model (CTEM; Arora and Boer, 2005; Melton and Arora, 2016). The physics and biogeochemistry components of CLASSIC are based on CLASS and CTEM, respectively. For the physics component, the default model's vegetation is represented in terms of the fractional coverage of the four PFTs (needleleaf trees, broadleaf trees, crops, and grasses). The physics component represents a single snow layer with variable depth and a single vegetation canopy layer. As a first-order treatment of subgrid-scale heterogeneity, each grid cell is divided up into four sub-areas, consisting of vegetated and bare soil areas, each with and without snow cover. The visible and near-infrared albedos of each PFT/vegetation category are specified. These albedos are further modified by taking into account the fraction of the ground that is seen from the sky above referred to as the sky view factor (which is modelled as a function of the leaf area index). The albedo of the ground that is seen from the sky above depends on if the ground is snow covered or not but also on the soil moisture of the top soil layer, since wet soil is darker than the dry soil. Canopy snow processes such as interception/unloading, sublimation, and melt are all simulated. The aggregated visible and near-infrared albedos for the bulk canopy are incremented using the current values weighted by the fractional coverage of the vegetation categories (Verseghy, 1993). More details can be found in Appendix A. The overall surface albedo of a grid cell is computed as a weighted mean using the fractional coverages for the four sub-areas. Twenty ground layers represent the soil profile, starting with 10 layers of 0.1 m thickness. The thicknesses of the layers gradually increase to 30 m for a total ground depth of over 61 m. Liquid and frozen soil moisture contents, and soil temperature, are determined prognostically for permeable soil layers. The biogeochemistry component of CLASSIC used here represents vegetation in terms of nine PFTs: needleleaf evergreen trees (NLE), needleleaf deciduous trees (NLD), broadleaf evergreen trees (BLE), broadleaf cold deciduous trees (BCD), broadleaf dry deciduous trees (BDD), C_3 and C_4 crops (C_3C/C_4C), and C_3 and C_4 grasses (C_3G/C_4G). These nine PFTs map directly onto the four PFTs used by CLASSIC's physics component. When the physics and biogeochemistry components are coupled together, as in the case of simulations carried out in this study, the structural attributes of vegetation including leaf area index, canopy mass, rooting depth, and vegetation height are simulated dynamically as a function of environmental conditions by the biogeochemistry component. When the biogeochemistry component is turned off, specified structural attributes of vegetation for use by the physics component are extracted from look-up tables.

2.4.2 Simulation setup

Gridded meteorological data based on the Climatic Research Unit (CRU) and Japanese reanalysis (JRA) (CRUJRA, https://crudata.uea.ac.uk/cru/data/hrg/, last access: July 2022) are used to drive CLASSIC simulations. The data are constructed by regridding data from the JRA and adjusting where possible to align with the CRU TS 4.05 data. The blended product from January 1901 to December 2020 has the 6-hourly temporal resolution of the reanalysis product but monthly means adjusted to match the CRU data (Harris, 2020). The 6-hourly data are disaggregated on the fly within CLASSIC into half-hourly data following the methodology by Melton and Arora (2016) for the following seven meteorological variables that are used to force the model: 2 m air temperature, total precipitation, specific humidity, downward solar radiation flux, downward longwave radiation flux, surface pressure, and wind speed. Surface temperature, surface pressure, specific humidity, and wind speed are linearly interpolated. Longwave radiation is uniformly distributed across a 6-hour period, and shortwave radiation is diurnally distributed over a day based on a grid cell's latitude and day of year with the maximum value occurring at solar noon. Precipitation is treated following Arora (1997), where the total 6 h precipitation amount is used to determine the number of wet half hours in a 6 h period. The 6 h precipitation amount is then spread randomly, but conservatively, over the wet half-hourly periods. In CLASSIC, the phase of precipitation is determined by a threshold surface air temperature with three options available (Bartlett et al., 2006). The 0 °C air temperature threshold is used to partition precipitation into rain or snow in this study. This choice does not have a significant impact on the simulated surface albedo in CLASSIC especially during the February–March months when the snow cover is near its maximum (Wang et al., 2014).

Two simulations over the 1850–2020 historical period are performed using PFTs derived from the ESA-CCI and the GLC2000 datasets respectively, which is the only difference between the two simulations. Static PFTs are used in the simulations where the fractional coverage of PFTs is prescribed and does not vary through time. Besides land cover and meteorological forcings, CLASSIC requires globally averaged atmospheric CO_2 concentration and geographically varying time-invariant soil texture and soil permeable depth. The atmospheric CO_2 concentration values are provided by the Global Carbon Project protocol (Friedlingstein et al., 2019). The soil texture information consists of the percentage of sand, clay, and organic matter and is derived from the SoilGrids250m dataset (Hengl et al., 2017), and permeable soil depth is based on Shangguan et al. (2017). The simulations are performed at a 0.22° rotated latitude–longitude grid over a domain including Canada and part of Alaska

(Fig. 3). Pre-industrial simulations that correspond to the year 1850 are required prior to doing the historical simulations so that model's carbon pools, including leaf biomass which determines leaf area index, are spun up to near equilibrium for each land cover. The pre-industrial simulations use 1901–1920 meteorological data repeatedly with atmospheric CO_2 concentration specified at its 1850 level. Each historical simulation is then initialized from its corresponding pre-industrial simulation after it has reached equilibrium (with carbon fluxes to conditions corresponding to the year 1850). For the period 1851–1900, the CRUJRA meteorological data for the first 20 years (1901–1920) are used repeatedly. For the 1901–2020 period the meteorological data corresponding to each actual year are used. The period from 2001 to 2015 was selected for analyzing the simulated results.

3 PFT mapping methods

The CW-table for the ESA-CCI LC dataset is generated through a multi-step process that combines multiple land cover maps at different spatial and categorical resolutions with ancillary data on tree cover and vegetation height (Fig. 2). This includes the following steps:

1. combining two existing land cover maps (NALCMS and VLCE) to produce a harmonized 30 m land cover (hybrid) map with improved categorical precision (as described in Sect. 2.1);

2. creating a CW-table for the hybrid land cover map through a direct mapping of classes from the hybrid map onto the CLASSIC PFTs, such that each land cover class corresponds to a particular mix of PFTs as represented in CLASSIC. This step is supported by vegetation height data from an airborne lidar campaign over parts of Canada;

3. computing the sub-pixel fractional composition for classes in the ESA-CCI land cover map (300 m resolution) based on the 30 m hybrid land cover dataset and the Hansen tree cover fraction dataset;

4. using the sub-pixel fractional composition analysis to create a CW-table for mapping the ESA-CCI land cover classes onto PFTs as represented in CLASSIC; and

5. since the ESA-CCI dataset is global, the CW-table developed over Canada is extended to the whole globe.

3.1 CW-table for mapping hybrid LC classes to CLASSIC PFTs

Among the nine CLASSIC PFTs, BLE and BDD forests are not present in Canada. These are primarily tropical PFTs as represented in CLASSIC. NLD accounts for less than 1 % of coniferous forests in Canada (Wang et al., 2019). Therefore, we do not consider NLD, BLE, and BDD from here on in this study. Considering the fine resolution (30 m) of the hybrid map, especially relative to the model resolution ($\sim$ 16 km) used in this study, we assign fractions of 1.0 to the two pure forest classes (LC210 and LC220), the cropland (LC15), and the five non-vegetative classes (LC16 to LC32) in its CW-table (Table 1). The mixed-wood category (LC230) is split evenly into NLE and BCD in the table based on the definition in the VLCE legend (Hermosilla et al., 2018; Wulder et al., 2003). Note that in Table 1, broadleaf deciduous trees (BDD and BCD) are considered together and separated later into their cold and drought deciduous versions. Similarly, crops and grasses (C_3 and C_4) are considered together and separated later into their C_3 and C_4 varieties. The reason for this is that the separation of broadleaf trees into their cold and deciduous phenotypes is based on latitude (Wang et al., 2006). The separation of crops and grasses based on their photosynthetic pathway (C_3 or C_4) is done based on the C_4 fraction from Still and Berry (2003), which is available at 1° resolution.

CLASSIC explicitly represents shrub PFTs (Meyer et al., 2021), but this work does not use that model version, and therefore the fraction of tall shrubs is assigned to one of the tree PFTs as was done in creating the CW-table for GLC2000 for use with CLASSIC (Wang et al., 2006). Four (LC2 – sub-polar taiga needleleaf forest, LC50 – shrubland, LC80 – wetland, and LC81 – wetland–treed) out of the 17 classes in the hybrid map are characterized by a mosaic of trees, shrubs, and herbaceous vegetation. The vegetation coverage for canopy height above 2 m from lidar plots is used to inform the partitioning of forest (tall vegetation) to non-forest (low vegetation) fractions for these mixed classes. We overlay the lidar plots on the hybrid land cover map in ArcGIS. Samples (20 to 40, note that these classes do not cover large areas in Canada) for the four mixed classes in the hybrid map are selected where there are lidar data. The vegetation coverage data (for canopy height above 2 m) from lidar plots for samples of each class are used to compute an average coverage of tall vegetation ($>$ 2 m) for that class, which is then used to assign forest fractions for these four classes in Table 1.

The distribution of tree species from Beaudoin et al. (2014) is used to guide the separation of coniferous versus broadleaf forest fractions. For example, for the wetland–treed category (LC81), maps of tree species show that coniferous forests dominate wetland–treed regions, while broadleaf forests are generally non-existent. We, therefore, assign most of the forest fraction to NLE (0.55), only 0.05 to BCD, 0.35 to grasses, and the remaining to the bare ground for LC81 (Table 1). The presence of evergreen shrubs is rare in Canada according to National Forest Inventory ground plot data (Gillis et al., 2005); thus we only assign an estimated tall shrub fraction (0.20) in the shrub class (LC50) to BCD. The sub-polar or polar classes (LC11 to LC13) are located above the treeline and mainly consist of low shrubs and grass.

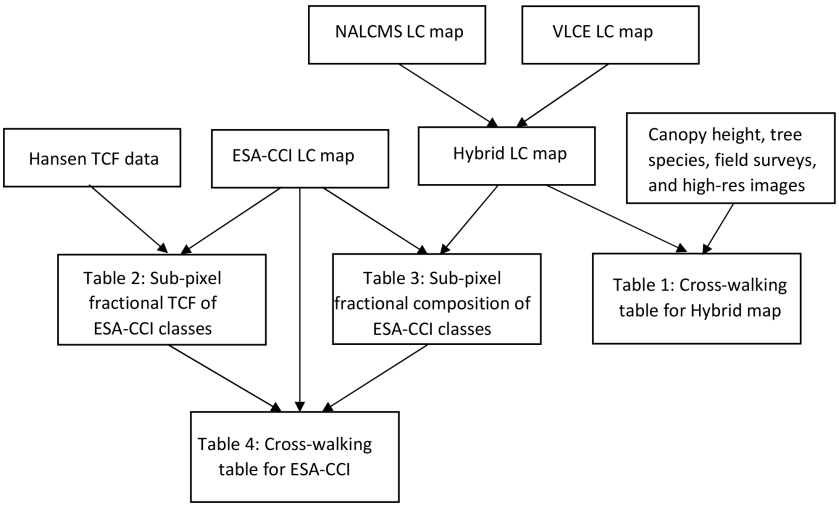

Figure 2. Schematic flow chart of the process for creating the cross-walking table for ESA-CCI land cover (LC) dataset. NALCMS: the North America Land Change Monitoring System; VLCE: the Virtual Land Cover Engine; TCF: tree cover fraction.

The fractions of grass (including low shrubs) and bare ground are based on field surveys of fractional vegetation cover and tundra PFT data in Bjorkman et al. (2018) and Macander et al. (2020) (by computing the average fractions at the field sites which overlap with the sub-polar or polar classes in the hybrid/NALCMS land cover map). High-resolution images from Google Earth engine or Bing Maps are also used to examine the ratio of vegetated versus bare ground for all classes in which bare ground is present.

3.2 CW-table for mapping ESA-CCI LC classes to CLASSIC PFTs over Canada

3.2.1 The error and sub-pixel fractional error matrices

A standard approach for the accuracy assessment of LC products is to use an error matrix. It is a square array or table of numbers arranged in rows and columns, in which the classification from the LC product (usually represented by the rows) is compared to the reference data (usually represented by the columns) for each category (Congalton, 1991). The major diagonal of the matrix presents the number of correct classifications indicating the agreement between the LC and the reference data for each category. In practice, fine-resolution regional maps are often used to assess large-scale LC products derived from coarse-resolution data (Cihlar et al., 2003). In such cases, the fine-resolution reference data are aggregated/regridded to match the grid of the coarse-resolution data. Several classes in the reference data may be present in a single coarse-resolution pixel depending on the homogeneity of the landscape. In order to compare the reference and the LC data on a one-to-one basis, the dominant LC class (the class with the most abundant fractions based on all fine-resolution pixels in the reference data) is often assigned to the regridded reference pixel.

The sub-pixel fractional error matrices have been introduced as a more appropriate way of assessing the accuracy of mixed pixels by Latifovic and Olthof (2004). In contrast with an error matrix where only the dominant LC class is used as described above, the sub-pixel fractional error matrix is produced by assigning sub-dominant LC classes from all fine-resolution pixels in the reference data to the corresponding single coarse-resolution pixel. It thus allows a quantitative assessment of the fractional composition of the LC classes in the coarse-resolution dataset. In this study, both the 30 m Hansen TCF data and the 30 m hybrid LC map are used to compute the sub-pixel fractional error matrices of the 300 m ESA-CCI dataset (Tables 2 and 3). However, the objective here is not an accuracy assessment as in Latifovic and Olthof (2004) but rather to obtain the fractional composition of the LC classes in the ESA-CCI product and to inform the PFT mapping process. We refer to this process as the sub-pixel fractional composition analysis in the rest of this paper. Sub-pixel fractional composition analyses are first performed for each ecozone, and then weighted mean fractions for each ESA-CCI class are computed based on pixel counts in each of the ecozones (see the location of ecozones in Fig. 1).

For the Hansen TCF data, results are shown only for the ESA-CCI LC classes containing forests in Canada (Table 2). In the ESA-CCI legend (Table 4), two sub-classes for broadleaf (LC61 and LC62) and needleleaf (LC71 and LC72) forests are included as the closed ($> 40\,\%$ forest cover) and open ($10\,\%$–$40\,\%$ forest cover) categories apart from the main classes (LC60 and LC70, closed to open ($> 15\,\%$)). As expected, the TCF is larger for the closed classes than for the main and the open classes (Table 2). In Table 2, we also include ratios of TCF between the main class and the closed class, and between the open class and the closed class. We note that the ratios are different for broadleaf

Table 1. Cross-walking table for mapping the 30 m hybrid land cover map to CLASSIC PFTs in Canada. Nine PFTs in CLASSIC: NLE – needleleaf evergreen trees, NLD – needleleaf deciduous trees, BLE – broadleaf evergreen trees, BCD – broadleaf cold deciduous trees, BDD – broadleaf dry deciduous trees, C_3C-C_3 crops, C_4C–C_4 crops, C_3G–C_3 grasses, and C_4C–C_4 grasses.

ID	Map description	1 NLE	2 NLD	3 BLE	4 + 5 BCD BDD	6 + 7 C_3C C_4C	8 + 9 C_3G C_4G	Urban	Lake	Bare
2	Sub-polar taiga needleleaf forest	0.20					0.60			0.20
11	Sub-polar or polar shrubland–lichen–moss						0.65			0.35
12	Sub-polar or polar grassland–lichen–moss						0.45			0.55
13	Sub-polar or polar barren–lichen–moss						0.10			0.90
15	Cropland					1.0				
16	Barren lands									1.0
17	Urban							1.0		
20	Water								1.0	
31	Snow/ice									1.0
32	Rock/rubble									1.0
50	Shrubland				0.20		0.60			0.20
80	Wetland				0.05		0.85			0.10
81	Wetland–treed	0.55			0.05		0.35			0.05
100	Herbs						0.80			0.20
210	Coniferous	1.0								
220	Broadleaf				1.0					
230	Mixed wood	0.50			0.50					

(main class vs. closed class: $68.5/86.7 = 0.8$; open class vs. closed class: $0.43/86.7 = 0.43$) and needleleaf (main class vs. closed class: $39.3/61.7 = 0.6$; open class vs. closed class: $23.2/61.7 = 0.38$) forests, which need to be taken into account when creating the CW-table for the ESA-CCI dataset.

To obtain representative class compositions of the ESA-CCI dataset, only homogenous ESA-CCI pixels are included in the sub-pixel composition analyses based on the hybrid LC data. The homogenous pixels are defined following the method in Herold et al. (2008). To quantify landscape heterogeneity, 3×3 pixel neighbourhoods are assessed for the ESA-CCI data. A neighbourhood is considered homogenous if only one LC class is present. The weighted mean fraction for each class is computed from ecozones with more than 10 homogenous ESA-CCI pixels for that class (Table 3). Only 13 out of the 37 ESA-CCI classes are included in Table 3; the rest of the classes either have limited presence in Canada or are non-vegetative (Table 4).

In the hybrid CW-table (Table 1), four LC classes (2, 81, 210, and 230) contribute to the fractional cover of NLE, and five LC classes (50, 80, 81, 220, and 230) contribute to the fractional cover of BCD. In Table 3, we also include an integrated fractional cover (F) for NLE and BCD (last two rows) for each of the ESA-CCI classes based on the following formula:

$$F = \sum_{i=1}^{N} F1_i \times F2_i, \quad (1)$$

where $F1_i$ are fractions in Table 3, $F2_i$ are fractions in Table 1, and N is the number of hybrid LC classes contributing to NLE ($N = 4$) or BCD ($N = 5$) as shown in Table 1. As an example, the fraction of NLE for the LC70 (tree cover

Table 2. The sub-pixel fractional tree cover fraction for ESA-CCI (European Space Agency – Climate Change Initiative) land cover classes (with forest cover) based on the Hansen TCF (tree cover fraction) dataset in Canada. Ratios of TCF between the main class and the closed class and between the open class and the closed class are also included.

ESA-CCI class	ESA-CCI class description	Tree cover fraction (%)	Ratio of TCF relative to closed class
30	Mosaic cropland (> 50 %)/natural vegetation (< 50 %)	13.7	
40	Mosaic natural vegetation (> 50 %)/cropland (< 50 %)	45	
60	Tree cover broadleaved deciduous closed to open (> 15 %)	68.5	0.8
61	Tree cover broadleaved deciduous closed (> 40 %)	86.7	1
62	Tree cover broadleaved deciduous open (15 %–40 %)	37.4	0.43
70	Tree cover needleleaf evergreen closed to open (> 15 %)	39.3	0.6
71	Tree cover needleleaf evergreen, closed (> 40 %)	61.7	1
72	Tree cover needleleaf evergreen open (15 %–40 %)	23.2	0.38
90	Tree cover mixed	80.9	
100	Mosaic tree and shrub (> 50 %)/herbaceous cover (< 50 %)	37.3	
110	Mosaic herbaceous cover (> 50 %)/tree and shrub (< 50 %)	19.6	
120	Shrubland	28.1	
150	Sparse vegetation (tree shrub herbaceous cover) (< 15 %)	4	
160	Tree cover, flooded fresh/brackish	43	
180	Shrub or herbaceous cover, flooded	26.9	

Table 3. The sub-pixel fractional composition for ESA-CCI classes (columns, homogenous ESA-CCI pixels) based on the hybrid land cover map (rows) for dominant land cover classes in Canada. The fractions for NLE and BCD are computed based on Eq. (1).

Hybrid/ ESA-CCI class	Hybrid description	30	40	60	70	71	90	100	120	130	140	150	160	180
2	Sub-polar taiga needleleaf forest				0.02			0.01		0.01				
11	Sub-polar/polar shrubland–lichen–moss										0.01	0.05		
12	Sub-polar/polar grassland–lichen–moss				0.04				0.03	0.01	0.24	0.27	0.03	0.04
13	Sub-polar/polar barren–lichen–moss				0.02			0.01	0.02	0.01	0.34	0.09		0.02
15	Cropland	0.92	0.37	0.02						0.1				
16	Barren lands									0.01	0.15	0.17		
50	Shrubland	0.01	0.07	0.06	0.13	0.05	0.04	0.32	0.46	0.09	0.14	0.25	0.06	
80	Wetland		0.03	0.08	0.2	0.05	0.03	0.27	0.2	0.02	0.06	0.09	0.37	0.75
81	Wetland–treed		0.01	0.01	0.17	0.07	0.03	0.11	0.12				0.43	0.15
100	Herbs	0.06	0.27	0.08	0.02		0.02	0.06	0.09	0.72	0.01	0.03	0.01	0.01
210	Coniferous		0.01	0.02	0.29	0.72	0.07	0.04	0.03		0.01	0.02	0.06	
220	Broadleaf	0.01	0.13	0.57	0.02	0.01	0.28	0.07	0.01	0.01			0.01	
230	Mixed wood		0.1	0.14	0.09	0.07	0.52	0.12	0.03				0.02	
NLE	Needleleaf evergreen		0.07	0.09	0.44	0.8	0.32	0.19	0.16	0.01	0.02	0.05	0.31	0.08
BCD	Broadleaf cold deciduous	0.01	0.19	0.66	0.09	0.06	0.57	0.18	0.09	0.02	0.02	0.03	0.05	0.03

needleleaf evergreen closed to open) in ESA-CCI data in Table 3 (see the NLE row and the column for class 70) is obtained as follows: $F = 0.02\times0.20+0.17\times0.55+0.29\times1.0+0.09\times0.5 = 0.44$. This process reduces the subjectivity in assigning the ESA-CCI land cover classes to CLASSIC's two tree PFTs (NLE and BCD) that are present in Canada since the process is based on the high-resolution hybrid LC data.

3.2.2 CW-table for the ESA-CCI LC dataset over Canada

Tables 2 and 3 thus form the basis for creating the CW-table for mapping the ESA-CCI LC classes to CLASSIC's PFTs (Fig. 2 and Table 4). For the ESA-CCI class LC61 (Tree cover broadleaved deciduous closed, not included in Table 3 due to limited presence in Canada), ratios of TCF for LC60 vs. LC61 in Table 2 and the fractions of LC60 (tree cover broadleaved deciduous closed to open) in Table 3 are used to derive fractions for LC61 in Table 4. The remapping of LC62 (tree cover broadleaved deciduous open) and LC72 (Tree cover needleleaf evergreen open) into CLASSIC's PFTs is done in a similar way. Since NLD is not included in either Table 2 or Table 3, the needleleaf deciduous tree cover classes (LC80-82) are assigned to the same fractions as the needleleaf evergreen tree cover classes (LC70-72). For simplicity, the fractions in Table 3 are rounded to values with either "0"

Table 4. Cross-walking table for mapping ESA-CCI land cover dataset to CLASSIC PFTs.

ID	ESA-CCI class description	1 NLE	2 NLD	3 BLE	4 + 5 BCD BDD	6 + 7 C_3C C_4C	8 + 9 C_3G C_4G	Urban	Lake	Ocean	Bare
10	Cropland, rainfed (CR)					0.80	0.20				
11	CR herbaceous cover					0.90	0.10				
12	CR tree or shrub cover				0.60		0.30				0.10
20	Cropland, irrigated, or post-flood				0.05	0.85	0.10				
30	Mosaic cropland (> 50 %)/natural vegetation (tree, shrub, herb)	0.05			0.15	0.60	0.20				
40	Mosaic natural vegetation (tree, shrub, herb) > 50 %/crop	0.10			0.20	0.40	0.30				
50	Tree cover broadleaved evergreen closed to open			0.95	0.05		0.0				
60	Tree cover broadleaved deciduous closed to open				0.70		0.25				0.05
61	Tree cover broadleaved deciduous closed				0.90		0.10				
62	Tree cover broadleaved deciduous open				0.40		0.40				0.20
70	Tree cover needleleaf evergreen closed to open	0.85			0.05		0.10				
71	Tree cover needleleaf evergreen, closed	0.85			0.05		0.10				
72	Tree cover needleleaf evergreen open	0.35			0.10		0.40				0.15
73	Replace LC70 in Canada	0.45			0.10		0.30				0.15
80	Tree cover needleleaf deciduous closed to open	0.05	0.40		0.10		0.35				0.10
81	Tree cover needleleaf deciduous closed	0.05	0.80		0.05		0.15				
82	Tree cover needleleaf deciduous open	0.05	0.30		0.10		0.45				0.15
90	Tree cover mixed	0.25	0.05		0.60		0.10				
100	Mosaic tree and shrub (> 50 %)/herbaceous cover (< 50 %)	0.15	0.05		0.20		0.45				0.15
110	Mosaic herbaceous cover (> 50 %)/tree and shrub (< 50 %)	0.05	0.05		0.10		0.65				0.15
120	Shrubland				0.30		0.45				0.25
121	Shrubland evergreen	0.15		0.15			0.45				0.25
122	Shrubland deciduous				0.30		0.45				0.25
130	Grassland						0.70				0.30
140	Lichens and mosses						0.20				0.80
150	Sparse vegetation (tree shrub herbaceous cover) (<15 %)				0.05		0.35				0.60
151	Sparse tree (<15 %)				0.05		0.35				0.60
152	Sparse shrub (<15 %)						0.30				0.70
153	Sparse herbaceous cover (<15 %)						0.30				0.70
160	Tree cover, flooded fresh/brackish	0.30			0.10		0.45		0.1		0.05
170	Tree cover, flooded saline water	0.30			0.10		0.40			0.1	0.10
180	Shrub or herbaceous cover, flooded	0.10			0.05		0.45		0.15	0.15	0.10
190	Urban areas	0.025			0.025		0.15	0.75	0.05		
200	Bare areas										1.0
201	Consolidated bare areas										1.0
202	Unconsolidated bare areas										1.0
210	Water bodies								1.0		
220	Permanent snow and ice										1.0

or "5" at the hundredth place when used in Table 4. For the rest of the classes not included in either Table 2 or Table 3, values are based on the default CW-table from the ESA-CCI user guide (Table 7-2, ESA, 2017). The spatial distribution of LC classes is also taken into consideration when determining the fractions in the CW-table. For example, the sparse vegetation class (LC150) is mainly distributed above the treeline in alpine and Arctic tundra environments. Thus we only assign 0.05 to BCD and the rest to C_3G/C_4G and bare ground (Table 4).

The six CLASSIC PFTs (those present in Canada) are produced from the hybrid and the ESA-CCI maps based on Tables 1 and 4 respectively. The PFTs from the hybrid map are used as a reference here to map ESA-CCI land cover classes to CLASSIC's PFTs. To make the spatial distribution of PFTs from ESA-CCI agree better with those from the hybrid dataset, fractions for the following classes in Table 4 are adjusted upward by 0.05: LC60 from 0.65 to 0.70 for BCD; LC71 and LC81 from 0.80 to 0.85 for NLE; and LC120 from 0.10 to 0.15 for BCD. Values for LC10-20 are also slightly adjusted to reduce crop fractions.

Based on Table 4, the fractional coverage of nine CLASSIC PFTs are also produced on a global scale and used in offline CLASSIC simulations in Arora et al. (2022), who carry out a comprehensive assessment of the impact of using two different LC datasets (ESA-CCI versus GLC2000) for representing the nine PFTs in the CLASSIC model. However, some adjustments to Table 4 are found to be necessary. This is because fractions of NLE (needleleaf evergreen forests) in Eurasia are found to be too low relative to the Hansen TCF data, with maximum values only around 0.45 in most NLE-dominated areas, where the maximum TCF from the Hansen dataset is around 0.80. This indicates that the needleleaf evergreen forests classes (LC 70–72) in the ESA-CCI map may represent different forest/tree cover fractions in Canada and Eurasia, which is confirmed by sub-pixel fractional composition analyses based on the Hansen TCF dataset. Details are presented in Appendix B.

4 Results

4.1 Comparison of PFTs from hybrid, ESA-CCI, and GLC2000 data

Figure 3 shows the spatial distribution of PFTs derived from the hybrid, ESA-CCI, and GLC2000 LC datasets respectively. C_4 crops (C_4C) and grasses (C_4G) are sparse in Canada as would be expected since C_4 PFTs grow only in warmer temperatures when the average monthly temperature exceeds 22 °C (Fox et al., 2018). Based on the fractional distribution of C_4 vegetation in Still and Berry (2003) and the hybrid map, the average fraction is 0.5 % for C_4 crops and 0.1 % for C_4 grasses in Canada. Therefore, only four out of the six PFTs (those present in Canada) are shown in Fig. 3. The C_4 fraction product from Still and Berry (2003) is available at a much coarser spatial resolution (1°) than other land cover products used in this study, and it is a global product. As such then, the estimated C_4 fractions for crops/grasses in Canada used here may not completely agree with those from regional estimates. In general, the spatial distributions of the PFTs from the ESA-CCI and the hybrid datasets agree well except for C_3 grasses (C_3G) (Fig. 3j and k). This is not surprising given that the CW-table for the ESA-CCI dataset is based on the hybrid map. Areas mapped as C_3G in hybrid (Fig. 3j) were mainly classified as sparse vegetation (LC150) in the ESA-CCI legend (Table 4). However, LC150 from ESA-CCI was also found in some areas of the high Arctic islands, where barren land is the dominant class in the hybrid map (grey coloured areas in Fig. 1). If too much grass were assigned to LC150, it would yield unrealistically large fractional coverage of grass in the high Arctic islands. In Table 4, for LC150, 0.05 is assigned to BCD, 0.35 to grasses, and the rest to the bare ground for LC150, which yields a total vegetation cover of 40 % and is more than the definition (< 15 % vegetation) used in the ESA-CCI legend. Yet, this still results in less C_3G and less bare ground in the ESA-CCI map (Fig. 3k and n) than those from the hybrid map (Fig. 3j and m). This suggests that it is not ideal to classify areas in the high Arctic islands and in the Arctic tundra region as being in the same land cover category.

There are large differences in the spatial distribution of the PFTs based on the GLC2000 LC product and those based on the hybrid and ESA-CCI datasets (Figs. 3 and 4). Relative to PFTs from ESA-CCI, GLC2000 has less NLE and more BCD in northwestern Canada and more NLE in southern and eastern Canada (Fig. 4a and b). GLC2000-based CLASSIC PFT fractions also exhibit more crops, less grass, and more bare ground (Fig. 4c–e). These differences partly stem from the differences in the ESA-CCI and GLC2000 LC datasets, but they are also due to how the fractions in the CW-tables of the two datasets are used to translate LC data to fractional coverage of PFTs as demonstrated in Wang et al. (2019).

4.2 Bias in simulated surface albedo and LAI

The top row of Fig. 5 shows the bias in winter albedo (March) simulated by CLASSIC when using PFT distributions based on the ESA-CCI (Fig. 5a) and GLC2000 products (Fig. 5b). While model biases are the result of both the driving geophysical and meteorological data that are used to force the model, as well as the model itself, the comparison between the two simulations does show the effect of differences in the distribution of PFTs. Relative to observed surface albedo from MODIS, there are relatively large negative biases in the southwest of Hudson Bay and central Quebec, while there are relatively large positive biases in western Canada and Alaska in the simulation when using the GLC2000 product to obtain PFT distributions (Fig. 5b). Both the negative and the positive biases are largely reduced in the simulation using

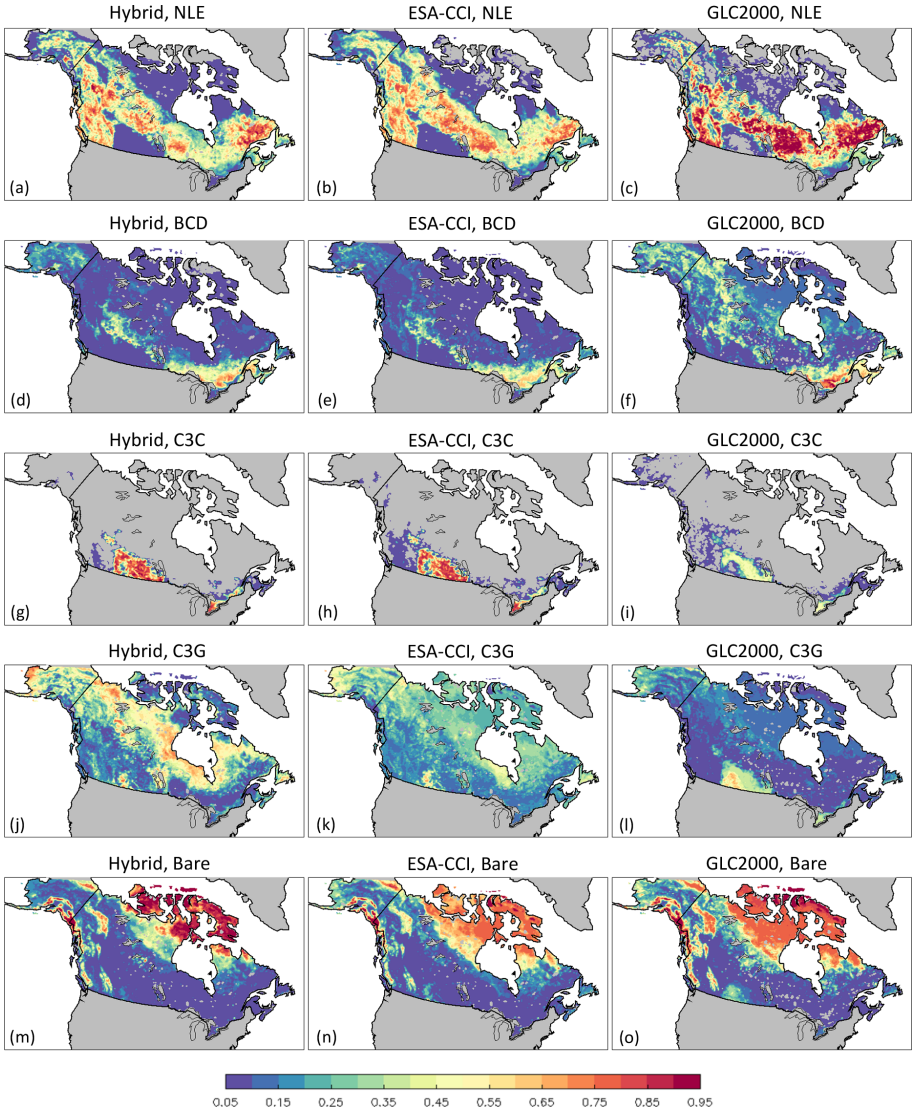

Figure 3. The spatial distribution of CLASSIC PFTs based on the hybrid (left), ESA-CCI (middle), and GLC2000 (right) land cover datasets respectively. The maps for C_4C and C_4G are not shown for their fractions are small (0.5 % for C_4 crops and 0.1 % for C_4 grasses) in Canada. The last panel shows fractions for bare ground from the three datasets.

PFT distributions based on the ESA-CCI product (Fig. 5a). The lower row of Fig. 5 shows the spatial distribution of the difference in surface albedo (Fig. 5c) and leaf area index (Fig. 5d) between the two simulations, which are closely correlated ($r = -0.85$). Given the same meteorological forcing dataset is used to drive both simulations, the differences in the simulated LAI are due mainly to the different PFT distributions used in the two simulations. Since NLE is the only PFT with LAI > 0 during winter in Canada, the LAI difference in March as shown in Fig. 5d is mainly due to the different fractional coverage of NLE based on the ESA-CCI and GLC2000 products (Fig. 4a).

In contrast, the large positive albedo biases (up to ~ 0.4) in southern Canada are more or less the same in both simulations (Fig. 5a and b), where the dominant PFT is C_3 crops (Fig. 3h and i). Those positive albedo biases are likely due to the standing crop stubble and the lack of the representation of blowing snow and its sublimation currently in CLASSIC (Harder et al., 2018; Pomeroy et al., 1993). Harder et al. (2018) showed that the height of the stubble over wheat and canola field in Saskatchewan, Canada, may range from 10 to 40 cm, with a maximum PAI (plant area index) of 1.0. Wang et al. (2016) showed that surface albedo in CLASSIC decreased exponentially with increasing PAI for the bare or snow-covered canopy over snow, while most reductions of the albedo were achieved through the increase of PAI from 0 to 1.0. They showed that surface albedo decreased from 0.75 to 0.31 in CLASSIC when PAI increased from 0 to 1.0 for the

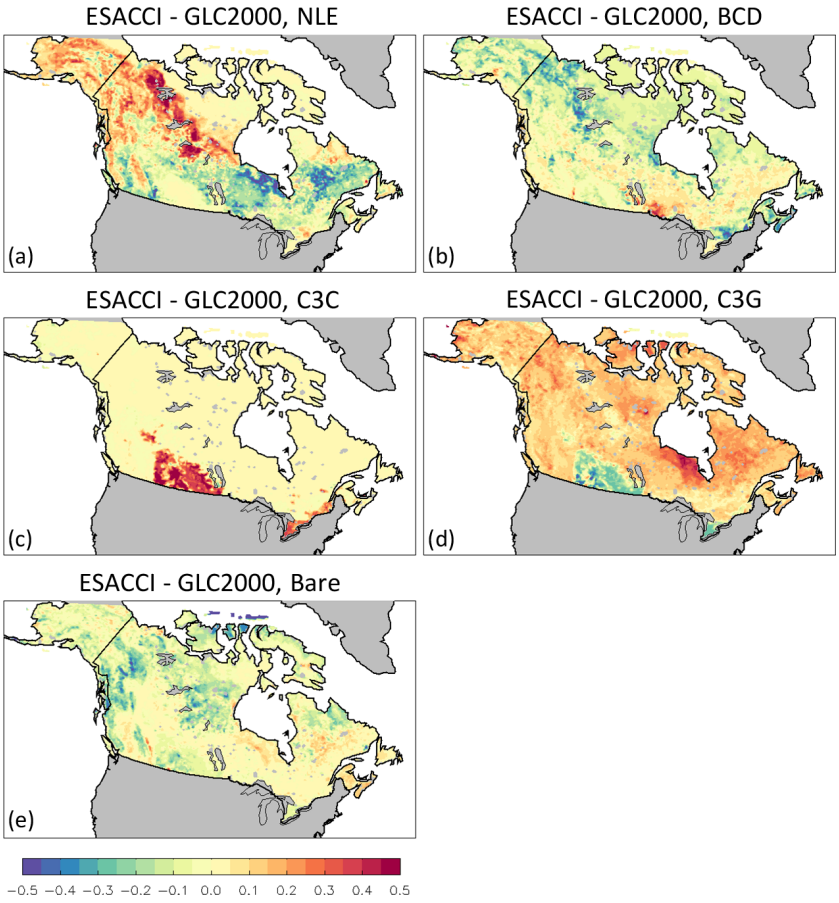

Figure 4. The difference in PFTs based on ESA-CCI and GLC2000 datasets for selected PFTs **(a)** NLE, **(b)** BCD, **(c)** C_3C, **(d)** C_3G, and **(e)** bare.

bare canopy over snow, which appears to account for most of the positive albedo biases in the agricultural areas of southern Canada (Fig. 5a and b). Improvements to the crop module of CLASSIC to improve cropland albedo are currently being considered.

5 Summary and conclusions

A hybrid land cover map at 30 m resolution is created by merging the NALCMS and VLCE land cover products over Canada. Vegetation height data from lidar plots, tree species, and high-resolution images are used to inform the creation of a CW-table for mapping the 17 LC classes of the hybrid map to six CLASSIC PFTs that are present in Canada. Both the hybrid map and the Hansen tree cover fraction data are used to compute the sub-pixel fractional composition of the LC classes in the ESA-CCI LC dataset, which is then used to create a cross-walking table for mapping the 37 ESA-CCI categories to CLASSIC PFTs over the model's Canadian domain. Based on the new CW-tables, PFT distributions are produced from the hybrid and the ESA-CCI LC products, respectively, and are compared with those based on the GLC2000 dataset currently used in CLASSIC. The results show that the spatial distribution of PFTs from the ESA-CCI dataset is in better agreement with those from the hybrid map, while there are large differences in the PFTs from the GLC2000 dataset and from the hybrid/ESA-CCI datasets. The CW-table developed over Canada is adjusted and used to map PFTs based on the ESA-CCI LC product for use in CLASSIC simulations at the global scale.

Our PFT mapping approach for the ESA-CCI dataset is mainly based on sub-pixel fractional composition analyses using the hybrid map and the Hansen tree cover fraction data, and therefore the accuracy of the latter two datasets affects the PFT mapping process. Some LC categories in the ESA-CCI legend either have limited presence or no presence in Canada, such as the needleleaf deciduous trees, broadleaf evergreen trees, and broadleaf dry deciduous trees, etc., and the sub-pixel fractional composition analyses therefore cannot be performed for these LC categories. The needleleaf deciduous tree cover classes are assigned to the same fractions as the needleleaf evergreen tree cover classes in the CW-table, and values based on the default CW-table from the ESA-CCI user guide are used for the other LC categories. Therefore,

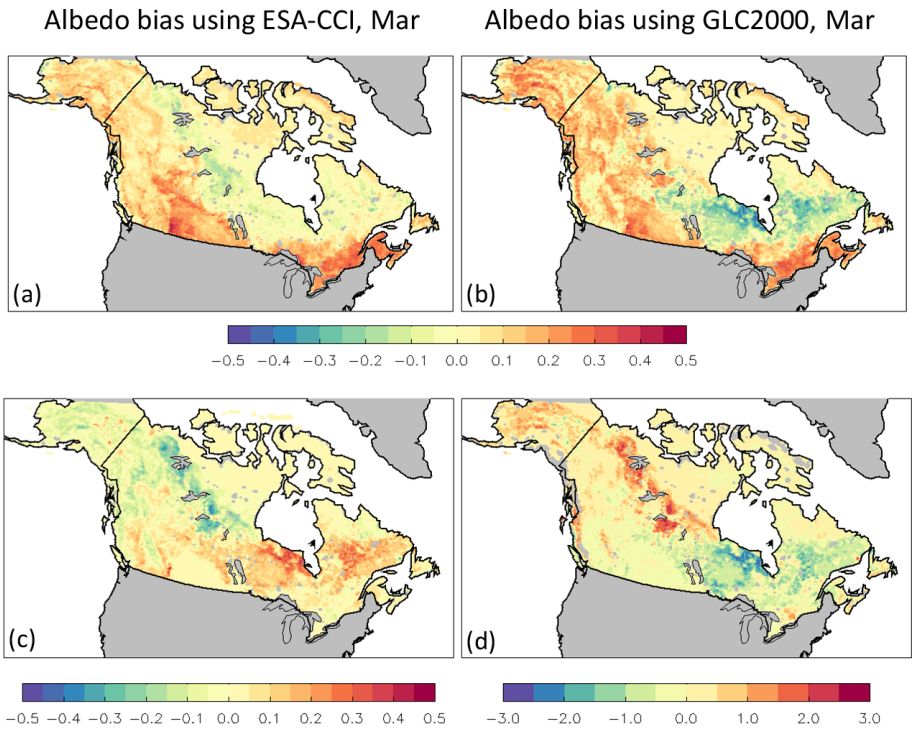

Figure 5. Surface albedo bias (relative to MODIS) in CLASSIC simulations using PFT distributions based on **(a)** ESA-CCI and **(b)** GLC2000 land cover products. Panels **(c)** and **(d)** show the difference in simulated surface albedo **(c)** and leaf area index **(d)** between the two simulations.

potentially large uncertainties may be associated with these classes in the resulting fractional coverage of PFTs especially at the global scale. Similar analyses for other regions (e.g. Eurasia and tropics) for which high-quality regional land cover maps are available will be helpful in reducing these uncertainties in the future work. In addition, the exercise of mapping PFTs at the global scale in this study reveals that there are inconsistencies in the representation of fractional coverage for some LC categories in the ESA-CCI map for different regions of the globe. Future improvements in the consistency of the LC categories globally in the ESA-CCI LC product would greatly benefit the land surface and the Earth system modelling community. In the meantime, caution should be exercised when using this product for mapping PFTs represented in any LSM based on a single cross-walking table at the global scale.

CLASSIC simulations driven with meteorological data from the CRU-JRA product show that the simulated winter albedo is improved when using PFT distributions based on the ESA-CCI LC product compared to that based on the GLC2000 product, which is consistent with findings from previous studies. While CLASSIC simulations could also have been performed using its PFT distributions based on the hybrid LC product, the reason for using the ESA-CCI-based PFT fractions for CLASSIC is that ESA-CCI is a global product. CLASSIC simulations are routinely performed at the global scale both in the framework of the Canadian Earth System Model (Swart et al., 2019), where CLASSIC serves as its land component, and offline where global CLASSIC simulations driven with the CRU-JRA meteorological data contribute to the annual global carbon budget assessments of the Global Carbon Project (Friedlingstein et al., 2020; Seiler et al., 2021). Untreated crop stubble appears to be contributing to the positive winter albedo biases in southern Canada, which needs to be addressed in a future version of CLASSIC. These results underscore the importance of accurate representation of vegetation distribution in a realistic simulation of surface albedo in LSMs.

Previous methods for mapping PFTs from LC datasets have mainly been based on class descriptions, expert knowledge, and the spatial distribution of global biomes, which is a largely subjective process. As a consequence, a PFT method developed for mapping one LC dataset to PFTs represented in one model cannot be easily transferred to other LC datasets even for deriving PFTs in the same model. The development of satellite and computing technology has enabled the creation of more detailed global LC products at finer spatial resolutions in recent years; however, the lack of an objective PFT mapping method impedes the implementation of the new improved LC products in LSMs. Here, we have proposed a method to inform the cross-walking process using sub-pixel fractional composition analyses based on a tree cover fraction dataset and a fine-resolution LC map. Our results suggest that the sub-pixel fractional composition anal-

yses provide an effective way to reduce uncertainties in the cross-walking process and therefore, to some extent, objectifies the otherwise subjective process. The PFT mapping approach developed in this study can also be applied to other LC datasets for mapping PFTs used in other LSMs.

Appendix A

In CLASSIC, the surface albedo for a canopy over snow (α) is

$$\alpha = \alpha_c (1-\chi)(1-f_{snow}) + \alpha_{c,\,snow}(1-\chi)(f_{snow}) + \alpha_{snow}\chi\tau_c \quad \text{(A1)}$$

$$\chi = \exp(-K \cdot PAI), \quad \text{(A2)}$$

calculated using separate parameters (α_c, $\alpha_{c,\,snow}$, τ_c and K) for both the visible (VIS) and near-infrared (NIR) bands, where α_c is the snow-free canopy albedo, $\alpha_{c,snow}$ the snow-covered canopy albedo, f_{snow} the fraction of the canopy with snow on it, and α_{snow} the snowpack albedo. τ_c is canopy transmissivity and is modelled using Beer's law approach, ignoring multiple reflections (Verseghy et al., 1993). K is an extinction coefficient that varies with vegetation type. The appearance of τ_c in the last term of Eq. (A1) accounts for the shading of the snowpack by the canopy, converting the simulated snowpack albedo to an effective value of the canopy gaps. PAI is plant area index which is the sum of leaf area index and stem area index.

Appendix B

Based on Table 4, the fractional coverage of nine CLASSIC PFTs is also produced on a global scale. However, some adjustments to Table 4 were found necessary. This is because fractions of NLE (needleleaf evergreen forests) in Eurasia are found to be too low relative to the Hansen TCF data, with maximum values of only around 0.45 in most NLE-dominated areas, where the maximum TCF from the Hansen dataset is around 0.80. Needleleaf evergreen forests are represented by LC classes 70 (closed to open), 71 (closed), and 72 (open). Examining the ESA-CCI LC map shows that in Eurasia nearly all needleleaf evergreen forests are classified as LC70 (closed to open), with only fewer than 400 pixels as LC71 (closed), and none as LC72 (open). In contrast, in Canada 36 % of needleleaf evergreen forests are classified as LC70 (closed to open), 64 % as LC71 (closed), and less than 1 % as LC72 (open). This is understandable given that subclasses were only assigned where surface samples were available (ESA, 2017). Sub-pixel fractional composition analyses of the ESA-CCI classes based on the Hansen TCF dataset show that in Eurasia TCF for LC70 (closed to open) is 66 % and for LC71 (closed) is 35 % (note the few pixels within this class). This is in contrast with those in Canada where the TCF for LC70 (closed to open) is 39 % and for LC71 (closed) is 62 %, explaining the too low NLE fractions in Eurasia when mapping PFTs based on Table 4 and also the too high TCF in northwestern Canada when mapping PFTs based on the default CW-table (Wang et al., 2018). In order to apply Table 4 globally, the original LC70 (closed to open) was split into two classes: LC73 (a new class), which is the same as LC70 over Canada (and zero everywhere else), and LC70 (revised), which is the same as before except zero over Canada. The fractions for the new LC70 class are made the same as for LC71 in Table 4, which applies to NLE outside of Canada. Essentially, the closed-to-open needleleaf forest LC70 class over Eurasia is treated as the closed needleleaf forest.

Code and data availability. More information about the CLASSIC land surface model and its Fortran code are available at https://cccma.gitlab.io/classic_pages/ (last access: July 2022, Melton, 2022). The VLCE LC map and the lidar plot data were from the Canadian Forest Service of Natural Resources Canada (https://opendata.nfis.org/mapserver/nfis-change_eng.html, last access: June 2021). The NALCMS LC map was from the Canada Centre for Remote Sensing (https://open.canada.ca/data/en/dataset/c688b87f-e85f-4842-b0e1-a8f79ebf1133, last access: May 2020). The MODIS albedo data were from the online data pool at the NASA Land Processes Distributed Active Archive Center (LP DAAC; https://lpdaac.usgs.gov/data_access, last access: July 2018). The tree cover fraction data were from the Global Land Analysis and Discovery laboratory in the Department of Geographical Sciences at the University of Maryland (https://glad.umd.edu/Potapov/TCC_2010/, last access: October 2018). The GLC2000 LC map was downloaded from the EU Science Lab (https://forobs.jrc.ec.europa.eu/products/glc2000/data_access.php, last access: September 2018). The ESA-CCI LC map was provided by ESA (https://www.esa-landcover-cci.org. last access: August 2017).

Author contributions. LW conceived and designed this research and wrote the majority of the manuscript. VKA contributed to the writing on the CLASSIC model description and simulation setup. PB contributed to discussions about the research. EC designed the reprojection/regridding method for all the satellite-derived datasets and computed the PFT data. SRC processed field surveys of vegetation cover data and helped with model simulations. VKA, EC, and SRC provided comments and suggestions on the entire paper.

Competing interests. The contact author has declared that none of the authors has any competing interests.

Disclaimer. Publisher's note: Copernicus Publications remains neutral with regard to jurisdictional claims in published maps and institutional affiliations.

Acknowledgements. We would like to thank Mike Brady (ECCC) for his help with data processing, Joe Melton (ECCC) for helpful comments on an early draft of the manuscript, and Mike Wulder

from the Canadian Forest Service of Natural Resources Canada for providing the lidar plot data and for helping interpret the lidar data and the VLCE land cover map. We also thank Benjamin Bond Lamberty for taking this paper on as an associate editor and the two anonymous reviewers for providing helpful comments, which greatly improved this paper.

Review statement. This paper was edited by Ben Bond-Lamberty and reviewed by two anonymous referees.

References

Arora, V.: Land surface modelling in general circulation models: a hydrological perspective, PhD thesis, Department of Civil and Environmental Engineering, University of Melbourne, 1997.

Arora, V. K. and Boer, G. J.: A parameterization of leaf phenology for the terrestrial ecosystem component of climate models, Glob. Chang. Biol., 11, 39–59, 2005.

Arora, V. K. and Boer, G. J.: Uncertainties in the 20th century carbon budget associated with land use change, Glob. Change Biol., 16, 3327–3348, https://doi.org/10.1111/j.1365-2486.2010.02202.x, 2010.

Arora, V. K., Boer, G. J., Christian, J. R., Curry, C. L., Denman, K. L., Zahariev, K., Flato, G. M., Scinocca, J. F., Merryfield, W. J., and Lee, W. G.: The Effect of Terrestrial Photosynthesis Down Regulation on the Twentieth-Century Carbon Budget Simulated with the CCCma Earth System Model, J. Climate, 22, 6066–6088, https://doi.org/10.1175/2009JCLI3037.1, 2009.

Arora, V. K., Seiler, C., Wang, L., and Kou-Giesbrecht, S.: Towards an ensemble-based evaluation of land surface models in light of uncertain forcings and observations, Biogeosciences, 20, 1313–1355, https://doi.org/10.5194/bg-20-1313-2023, 2023.

Bartholomé, E. and Belward, A. S.: GLC2000: A new approach to global land cover mapping from Earth Observation data, Int. J. Remote Sens., 26, 1959–1977, 2005.

Bartlett, P. A. and Verseghy, D. L.: Modified treatment of intercepted snow improves the simulated forest albedo in the Canadian land surface scheme, Hydrol. Process., 29, 3208–3226, https://doi.org/10.1002/hyp.10431, 2015.

Bartlett, P. A., MacKay, M. D., and Verseghy, D. L.: Modified snow algorithms in the Canadian land surface scheme: Model runs and sensitivity analysis at three boreal forest stands, Atmos.-Ocean, 44, 207–222, 2006.

Beaudoin, A., Bernier, P. Y., Guindon, L., Villemaire, P., Guo, X. J., Stinson, G., Bergeron, T., Magnussen, S., and Hall, R. J.: Mapping attributes of Canada's forests at moderate resolution through kNN and MODIS imagery, Can. J. For. Res., 44, 521–532, https://doi.org/10.1139/cjfr-2013-0401, 2014.

Betts, R. A.: Biogeophysical impacts of land use on present-day climate: near-surface temperature change and radiative forcing, Atmos. Sci. Lett., 2, 39–51, https://doi.org/10.1006/asle.2001.0037, 2001.

Bjorkman, A. D., Myers-Smith, I. H., Elmendorf, S. C., et al.: Plant functional trait change across a warming tundra biome, Nature, 562, 57–62, https://doi.org/10.1038/s41586-018-0563-7, 2018.

Bonan, G. B., Levis, S., Kergoat, L., and Oleson, K. W.: Landscapes as patches of plant functional types: An integrating concept for climate and ecosystem models, Global Biogeochem. Cy., 16, 1021, https://doi.org/10.1029/2000GB001360, 2002.

Bonan, G. B., Levis, S., Sitch, S., Vertenstein, M., and Oleson, K. W.: A dynamic global vegetation model for use with climate models: Concepts and description of simulated vegetation dynamics, Global Change Biol., 9, 1543–1566, 2003.

Bontemps, S., Herold, M., Kooistra, L., van Groenestijn, A., Hartley, A., Arino, O., Moreau, I., and Defourny, P.: Revisiting land cover observation to address the needs of the climate modeling community, Biogeosciences, 9, 2145–2157, https://doi.org/10.5194/bg-9-2145-2012, 2012.

Di Gregorio, A.: Land Cover Classification System – Classification concepts and user manual for Software version 2, FAO Environment and Natural Resources Service Series, No. 8, Rome, 208 pp., 2005.

ESA: Land Cover CCI Product User Guide Version 2. Tech. Rep., http://maps.elie.ucl.ac.be/CCI/viewer/download/ESACCI-LC-Ph2-PUGv2_2.0.pdf, last access: August 2017.

Fisher, R. A., Koven, C. D., Anderegg, W. R. L.,Christoffersen, B. O., Dietze, M. C., Farrior, C. E., Holm, J. A., Hurtt, G. C., Knox, R. G., Lawrence, P. J., Lichstein, J. W., Longo, M., Matheny, A. M., Medvigy, D., Muller-Landau, H. C., Powell, T. L., Serbin, S. P., Sato, H., Shuman, J. K., Smith, B., Trugman, A. T., Viskari, T., Verbeeck, H., Weng, E., Xu, C., Xu, X., Zhang, T., and Moorcroft P. R.: Vegetation demographics in Earth System Models: A review of progress and priorities. Global Change Biol., 24, 35–54, https://doi.org/10.1111/gcb.13910, 2018.

Fox, D. L., Pau, S., Taylor, L., Strömberg, C. A. E., Osborne, C. P., Bradshaw, C., Conn, S., Beerling, D. J., and Still, C. J.: Climatic Controls on C_4 Grassland Distributions During the Neogene: A Model-Data Comparison, Front. Ecol. Evol., 6, 147, https://doi.org/10.3389/fevo.2018.00147, 2018.

Friedlingstein, P., O'Sullivan, M., Jones, M. W., Andrew, R. M., Hauck, J., Olsen, A., Peters, G. P., Peters, W., Pongratz, J., Sitch, S., Le Quéré, C., Canadell, J. G., Ciais, P., Jackson, R. B., Alin, S., Aragão, L. E. O. C., Arneth, A., Arora, V., Bates, N. R., Becker, M., Benoit-Cattin, A., Bittig, H. C., Bopp, L., Bultan, S., Chandra, N., Chevallier, F., Chini, L. P., Evans, W., Florentie, L., Forster, P. M., Gasser, T., Gehlen, M., Gilfillan, D., Gkritzalis, T., Gregor, L., Gruber, N., Harris, I., Hartung, K., Haverd, V., Houghton, R. A., Ilyina, T., Jain, A. K., Joetzjer, E., Kadono, K., Kato, E., Kitidis, V., Korsbakken, J. I., Landschützer, P., Lefèvre, N., Lenton, A., Lienert, S., Liu, Z., Lombardozzi, D., Marland, G., Metzl, N., Munro, D. R., Nabel, J. E. M. S., Nakaoka, S.-I., Niwa, Y., O'Brien, K., Ono, T., Palmer, P. I., Pierrot, D., Poulter, B., Resplandy, L., Robertson, E., Rödenbeck, C., Schwinger, J., Séférian, R., Skjelvan, I., Smith, A. J. P., Sutton, A. J., Tanhua, T., Tans, P. P., Tian, H., Tilbrook, B., van der Werf, G., Vuichard, N., Walker, A. P., Wanninkhof, R., Watson, A. J., Willis, D., Wiltshire, A. J., Yuan, W., Yue, X., and Zaehle, S.: Global Carbon Budget 2020, Earth Syst. Sci. Data, 12, 3269–3340, https://doi.org/10.5194/essd-12-3269-2020, 2020.

Fritz, S., See, L., McCallum, I., Schill, C., Obersteiner, M., van der Velde, M., Boettcher, H., Havlík, P., and Achard, F.: Highlighting continued uncertainty in global land cover maps for the user community, Environ. Res. Lett., 6, 44005, https://doi.org/10.1088/1748-9326/6/4/044005, 2011.

Georgievski, G. and Hagemann, S.: Characterizing uncertainties in the ESA-CCI land cover map of the epoch 2010 and their impacts

on MPI-ESM climate simulations, Theor. Appl. Climatol., 137, 1587–1603, https://doi.org/10.1007/s00704-018-2675-2, 2019.

Gillis, M. D., Omule, A. Y., and Brierley, T.: Monitoring Canada's forests: The National Forest Inventory, The Forestry Chronicle, 81, 214–221, https://doi.org/10.5558/tfc81214-2, 2005.

Harris, I. C.: CRU JRA v2.1: A forcings dataset of gridded land surface blend of Climatic Research Unit (CRU) and Japanese reanalysis (JRA) data; Jan. 1901–Dec. 2019, Centre for Environmental Data Analysis, University of East Anglia Climatic Research Unit, https://catalogue.ceda.ac.uk/uuid/10d2c73e5a7d46f4ada08b0a26302ef7 (last access: July 2022), 2020.

Hartley, A. J., MacBean, N., Georgievski, G., and Bontemps, S.: Uncertainty in plant functional type distributions and its impact on land surface models, Remote Sens. Environ., 203, 71–89, https://doi.org/10.1016/j.rse.2017.07.037, 2017.

Harder, P., Warren D. H., and Pomeroy, J. W.: Modeling the Snowpack Energy Balance during Melt under Exposed Crop Stubble, J. Hydrometeorol., 19, 1191–1214, https://doi.org/10.1175/JHM-D-18-0039.1, 2018.

Hansen, M. C., DeFries, R. S., Townshend, J. R. G., Sohlberg, R., Dimiceli, C., Carroll, M. L.: Towards an operational MODIS continuous field of percent tree cover algorithm: Examples using AVHRR and MODIS data, Remote Sens. Environ., 83, 303–319, 2002.

Hansen, M. C., Stehman, S. V., and Potapov, P. V.: Quantification of global gross forest cover loss, P. Natl. Acad. Sci., 107, 8650–8655, https://doi.org/10.1073/pnas.0912668107, 2010.

Hansen, M. C., Potapov, P. V., Moore, R., Hancher, M., Turubanova, S. A., Tyukavina, A., Thau, D., Stehman, S. V., Goetz, S. J., Loveland, T.R., Kommareddy, A., Egorov, A., Chini, L., Justice, C. O., and Townshend, J. R. G.: Highresolution global maps of 21st-century forest cover change, Science, 342, 850–853, https://doi.org/10.1126/science.1244693, 2013.

Hengl, T., Mendes de Jesus, J., Heuvelink, G. B. M., Ruiperez Gonzalez, M., Kilibarda, M., Blagotić, A., Shangguan, W., Wright, M. N., Geng, X., Bauer-Marschallinger, B., Guevara, M. A., Vargas, R., MacMillan, R. A., Batjes, N. H., Leenaars, J. G. B., Ribeiro, E., Wheeler, I., Mantel, S., and Kempen, B.: SoilGrids250m: Global gridded soil information based on machine learning, PLOS ONE, 12, 1–40, https://doi.org/10.1371/journal.pone.0169748, 2017.

Hermosilla, T., Wulder, M. A., White, J. C., Coops, N. C., and Hobart, G. W.: Disturbance informed annual land cover classification maps of Canada's forested ecosystems for a 29-year Landsat time series, Can. J. Remote. Sens., 44, 67–87, https://doi.org/10.1080/07038992.2018.1437719, 2018.

Herold, M., Mayaux, P., Woodcock, C. E., BaESACCIni, A., and Schmullius, C.: Some Challenges in Global Land Cover Mapping: An Assessment of Agreement and Accuracy in Existing 1 km Datasets, Remote Sens. Environ., 112, 2538–2556, 2008.

Hopkinson, C., Chasmer, L., Lim, K., Treitz, P., and Creed, I.: Towards a universal lidar canopy height indicator, Can. J. Remote Sens., 32, 139–152, https://doi.org/10.5589/m06-006, 2006.

Krinner, G., Viovy, N., de Noblet-Ducoudre, N., Ogee, J., Polcher, J., Friedlingstein, P., Ciais, P., Sitch, S., and Prentice, I. C.: A dynamic global vegetation model for studies of the coupled atmosphere-biosphere system, Global Biogeochem. Cy., 19, GB1015, https://doi.org/10.1029/2003GB002199, 2005.

Latifovic, R., Pouliot, D., and Olthof, I.: Circa 2010 Land Cover of Canada: Local Optimization Methodology and Product Development, Remote Sens., 9, 1098, https://doi.org/10.3390/rs9111098, 2017.

Latifovic, R. and Olthof, I.: Accuracy assessment using sub-pixel fractional error matrices of global land cover products derived from satellite data, Remote Sens. Environ., 90, 153–165, 2004.

Macander, M. J., Frost, G. V., Nelson, P. R., and Swingley, C. S.: ABoVE: Tundra Plant Functional Type Continuous-Cover, North Slope, Alaska, 2010–2015, ORNL DAAC, Oak Ridge, Tennessee, USA, https://doi.org/10.3334/ORNLDAAC/1830, 2020.

Mayaux, P., Eva, H., Gallego, J., Strahler, A. H., Herold, M., Agrawal, S., Naumov, S., De Miranda, E. E., Di Bella, C. M., Ordoyne, C., Kopin, Y., and Roy, P. S.: Validation of the Global Land Cover 2000 Map, IEEE T. Geosci. Remote Sens., 44, 1728–1739, 2006.

Melton, J.: Model code for the Canadian Land Surface Scheme Including Biogeochemical Cycles (CLASSIC), [code], https://cccma.gitlab.io/classic_pages/, last access: July 2022.

Melton, J. R. and Arora, V. K.: Competition between plant functional types in the Canadian Terrestrial Ecosystem Model (CTEM) v. 2.0, Geosci. Model Dev., 9, 323–361, https://doi.org/10.5194/gmd-9-323-2016, 2016.

Melton, J. R., Arora, V. K., Wisernig-Cojoc, E., Seiler, C., Fortier, M., Chan, E., and Teckentrup, L.: CLASSIC v1.0: the open-source community successor to the Canadian Land Surface Scheme (CLASS) and the Canadian Terrestrial Ecosystem Model (CTEM) – Part 1: Model framework and site-level performance, Geosci. Model Dev., 13, 2825–2850, https://doi.org/10.5194/gmd-13-2825-2020, 2020.

Meyer, G., Humphreys, E. R., Melton, J. R., Cannon, A. J., and Lafleur, P. M.: Simulating shrubs and their energy and carbon dioxide fluxes in Canada's Low Arctic with the Canadian Land Surface Scheme Including Biogeochemical Cycles (CLASSIC), Biogeosciences, 18, 3263–3283, https://doi.org/10.5194/bg-18-3263-2021, 2021.

Moody, E. G., King, M. D., Schaaf, C. B., Hall, D. K., and Platnick, S.: Northern Hemisphere five-year average (2000–2004) spectral albedos of surfaces in the presence of snow: statistics computed from Terra MODIS land products, Remote Sens. Environ., 111, 337–345, https://doi.org/10.1016/j.rse.2007.03.026, 2007.

Ottlé, C., Lescure, J., Maignan, F., Poulter, B., Wang, T., and Delbart, N.: Use of various remote sensing land cover products for plant functional type mapping over Siberia, Earth Syst. Sci. Data, 5, 331–348, https://doi.org/10.5194/essd-5-331-2013, 2013.

Pielke, R. A., Avissar, R., Raupach, M., Dolman, A. J., Zeng, X., and Denning, S.: Interactions between the atmosphere and terrestrial ecosystem: influence on weather and climate, Global Change Biol., 4, 461–475, 1998.

Poulter, B., Ciais, P., Hodson, E., Lischke, H., Maignan, F., Plummer, S., and Zimmermann, N. E.: Plant functional type mapping for earth system models, Geosci. Model Dev., 4, 993–1010, https://doi.org/10.5194/gmd-4-993-2011, 2011.

Poulter, B., MacBean, N., Hartley, A., Khlystova, I., Arino, O., Betts, R., Bontemps, S., Boettcher, M., Brockmann, C., Defourny, P., Hagemann, S., Herold, M., Kirches, G., Lamarche, C., Lederer, D., Ottlé, C., Peters, M., and Peylin, P.: Plant functional type classification for earth system models: results from the European Space Agency's Land Cover Climate Change Initiative,

Geosci. Model Dev., 8, 2315–2328, https://doi.org/10.5194/gmd-8-2315-2015, 2015.

Pomeroy, J. W., Gray, D. M., and Landine, P. G.: The Prairie Blowing Snow Model: Characteristics, validation, operation, J. Hydrol., 144, 165–192, https://doi.org/10.1016/0022-1694(93)90171-5, 1993.

Schaaf, C. B., Gao, F., Strahler, A. H., Lucht, W., Li, X., Tsang, T., Strugnell, N. C., Zhang, X., Jin, Y., Muller, J. P., Lewis, P., Barnsley, M., Hobson, P., Disney, M., Roberts, G., Dunderdale, M., Doll, C., d'Entremont, R. P., Hu, B., Liang, S., Privette, J. F., and Roy, D.: First operational BRDF, albedo nadir reflectance products from MODIS, Remote Sens. Environ., 83, 135–148, https://doi.org/10.1016/S0034-4257(02)00091-3, 2002.

Scheiter, S., Langan, L., and Higgins, S. I.: Next-generation dynamic global vegetation models: learning from community ecology, New Phytol., 198, 957–969, https://doi.org/10.1111/nph.12210, 2013.

Seiler, C., Melton, J. R., Arora, V. K., and Wang, L.: CLASSIC v1.0: the open-source community successor to the Canadian Land Surface Scheme (CLASS) and the Canadian Terrestrial Ecosystem Model (CTEM) – Part 2: Global benchmarking, Geosci. Model Dev., 14, 2371–2417, https://doi.org/10.5194/gmd-14-2371-2021, 2021.

Shangguan, W., Hengl, T., Mendes de Jesus, J., Yuan, H., and Dai, Y.: Mapping the global depth to bedrock for land surface modeling, J. Adv. Model. Earth Syst., 9, 65–88, https://doi.org/10.1002/2016MS000686, 2017.

Smith, T. M., Shugart, H. H., and Woodward, F. I.: Plant functional types: their relevance to ecosystem properties and global change, Cambridge University Press, New York, 369 pp., 1997.

Smith, B., Prentice, I. C., and Sykes, M. T. : Representation of vegetation dynamics in the modelling of terrestrial ecosystems: Comparing two contrasting approaches within European climate space, Global Ecol. Biogeo., 10, 621–637, 2001.

Sterling, S. M., Ducharne, A., and Polcher, J.: The impact of global land-cover change on the terrestrial water cycle, Nat. Clim. Chang., 3, 385–390, https://doi.org/10.1038/nclimate1690, 2013.

Still, C. J. and Berry, J. A.: Global distribution of C_3 and C_4 vegetation: Carbon cycle implications, Global Biogeochem. Cycles, 17, 1006, https://doi.org/10.1029/2001GB001807, 2003.

Sun, W., Liang, S., Xu, G., Fang, H., and Dickinson, R. E.: Mapping plant functional types from MODIS data using multisource evidential reasoning, Remote Sens. Environ., 112, 1010–1024, https://doi.org/10.1016/j.rse.2007.07.022, 2008.

Swart, N. C., Cole, J. N. S., Kharin, V. V., Lazare, M., Scinocca, J. F., Gillett, N. P., Anstey, J., Arora, V., Christian, J. R., Hanna, S., Jiao, Y., Lee, W. G., Majaess, F., Saenko, O. A., Seiler, C., Seinen, C., Shao, A., Sigmond, M., Solheim, L., von Salzen, K., Yang, D., and Winter, B.: The Canadian Earth System Model version 5 (CanESM5.0.3), Geosci. Model Dev., 12, 4823–4873, https://doi.org/10.5194/gmd-12-4823-2019, 2019.

Tsendbazar, N. E., de Bruin, S., Mora, B., Schouten, L., and Herold, M.: Comparative assessment of thematic accuracy of GLC maps for specific applications using existing reference data, Int. J. Appl. Earth Obs. Geoinf., 44, 124–135, https://doi.org/10.1016/j.jag.2015.08.009, 2016.

Wang, A., Price, D. T., and Arora, V. K.: Estimating changes in global vegetation cover (1850–2100) for use in climate models, Global Biogeochem. Cy., 20, GB3028, https://doi.org/10.1029/2005GB002514, 2006.

Wang, L., MacKay, M., Brown, R., Bartlett, P., Harvey, R., and Langlois, A.: Application of satellite data for evaluating the cold climate performance of the Canadian Regional Climate model over Québec, Canada, J. Hydrometeorol., 15, 614–630, https://doi.org/10.1175/JHM-D-13-086.1, 2014.

Wang, L., Cole, J. N. S., Bartlett, P., Verseghy, D., Derksen, C., Brown, R., and von Salzen, K.: Investigating the spread in surface albedo for snow-covered forests in CMIP5 models, J. Geophys. Res.-Atmos., 121, 1104–1119, https://doi.org/10.1002/2015JD023824, 2016.

Wang, L., Bartlett, P., Chan, E., and Xiao, M.: Mapping of Plant Functional Type from Satellite-Derived Land Cover Datasets for Climate Models, In Proceedings of the 2018 IEEE International Geoscience and Remote Sensing Symposium, Valencia, Spain, 22–27, https://doi.org/10.1109/IGARSS.2018.8518046, 2018.

Wang, L., Bartlett, P., Pouliot, D., Chan, E., Lamarche, C., Wulder, M. A., Defourny, P., and Brady, M.: Comparison and Assessment of Regional and Global Land Cover Datasets for Use in CLASS over Canada, Remote Sens., 11, 2286, https://doi.org/10.3390/rs11192286, 2019.

Wulder, M. A. and Nelson, T.: EOSD land cover classification legend report: Version 2, Natural Resources Canada, Canadian Forest Service, Pacific Forestry Centre, Victoria, British Columbia, Canada, 13 January 2003, 83 pp., http://www.pfc.forestry.ca/eosd/cover/EOSD_Legend_Report-v2.pdf (last access: June 2021), 2003.

Wulder, M. A., Bater, C. W., Coops, N. C., Hilker, T., and White, J. C.: The role of LiDAR in sustainable forest management, The Forestry Chronicle, 84 807–826, 2008.

Wulder, M. A., White, J. C., Bater, C. W., Coops, N. C., Hopkinson, C., and Chen, G.: Lidar plots – a new large-area data collection option: context, concepts, and case study, Can. J. Remote. Sens., 38, 600–618, https://doi.org/10.5589/m12-049, 2012.

Verseghy, D. L.: CLASS – A Canadian Land Surface Scheme for GCMs, I. Soil model, Int. J. Climatol., 11, 111–133, https://doi.org/10.1002/joc.3370110202, 1991.

Verseghy, D., McFarlane, N., and Lazare, M.: Class – A Canadian land surface scheme for GCMs, II: Vegetation model and coupled runs, Int. J. Climatol., 13, 347–370, https://doi.org/10.1002/joc.3370130402, 1993.

Zakharova, L., Meyer, K. M., and Seifan, M.: Trait-based modelling in ecology: A review of two decades of research, Ecol. Model., 407, 108703, https://doi.org/10.1016/j.ecolmodel.2019.05.008, 2019.